remote sensing

MDPI

Technical Note

Spatiotemporal Variability of Global Atmospheric Methane Observed from Two Decades of Satellite Hyperspectral Infrared Sounders

Lihang Zhou [1], Juying Warner [2,*], Nicholas R. Nalli [3,4], Zigang Wei [3], Youmi Oh [5], Lori Bruhwiler [5], Xingpin Liu [3], Murty Divakarla [3,4], Ken Pryor [4], Satya Kalluri [1] and Mitchell D. Goldberg [6]

1 NOAA JPSS Program Office, Silver Spring, MD 20706, USA; lihang.zhou@noaa.gov (L.Z.); satya.kalluri@noaa.gov (S.K.)
2 Department of Atmospheric & Oceanic Science, University of Maryland, College Park, MD 20742, USA
3 IM Systems Group, Inc., 3206 Tower Oaks, Blvd., Suite 300, Rockville, MD 20852, USA; nick.nalli@noaa.gov (N.R.N.); zigang.wei@noaa.gov (Z.W.); xingpin.liu@noaa.gov (X.L.); murty.divakarla@noaa.gov (M.D.)
4 NOAA/NESDIS Center for Satellite Applications and Research (STAR), 5830 University Research Court, College Park, MD 20740, USA; ken.pryor@noaa.gov
5 NOAA Global Monitoring Laboratory (GML), 325 Broadway R/GML, Boulder, CO 80305, USA; youmi.oh@noaa.gov (Y.O.); lori.bruhwiler@noaa.gov (L.B.)
6 NOAA/NESDIS, 1335 East West Highway, Silver Spring, MD 20910, USA; mitch.goldberg@noaa.gov
* Correspondence: juying@atmos.umd.edu

Abstract: Methane (CH_4) is the second most significant contributor to climate change after carbon dioxide (CO_2), accounting for approximately 20% of the contributions from all well-mixed greenhouse gases. Understanding the spatiotemporal distributions and the relevant long-term trends is crucial to identifying the sources, sinks, and impacts on climate. Hyperspectral thermal infrared (TIR) sounders, including the Atmospheric Infrared Sounder (AIRS), the Cross-track Infrared Sounder (CrIS), and the Infrared Atmospheric Sounding Interferometer (IASI), have been used to measure global CH_4 concentrations since 2002. This study analyzed nearly 20 years of data from AIRS and CrIS and confirmed a significant increase in CH_4 concentrations in the mid-upper troposphere (around 400 hPa) from 2003 to 2020, with a total increase of approximately 85 ppb, representing a +4.8% increase in 18 years. The rate of increase was derived using global satellite TIR measurements, which are consistent with in situ measurements, indicating a steady increase starting in 2007 and becoming stronger in 2014. The study also compared CH_4 concentrations derived from the AIRS and CrIS against ground-based measurements from NOAA Global Monitoring Laboratory (GML) and found phase shifts in the seasonal cycles in the middle to high latitudes of the northern hemisphere, which is attributed to the influence of stratospheric CH_4 that varies at different latitudes. These findings provide insights into the global budget of atmospheric composition and the understanding of satellite measurement sensitivity to CH_4.

Keywords: hyperspectral IR sounding; CH_4; AIRS; CrIS; satellite measurement sensitivity; greenhouse gases; carbon trace gases; methane

check for updates

Citation: Zhou, L.; Warner, J.; Nalli, N.R.; Wei, Z.; Oh, Y.; Bruhwiler, L.; Liu, X.; Divakarla, M.; Pryor, K.; Kalluri, S.; et al. Spatiotemporal Variability of Global Atmospheric Methane Observed from Two Decades of Satellite Hyperspectral Infrared Sounders. *Remote Sens.* **2023**, *15*, 2992. https://doi.org/10.3390/rs15122992

Academic Editor: Carmine Serio

Received: 5 May 2023
Revised: 31 May 2023
Accepted: 5 June 2023
Published: 8 June 2023

Copyright: © 2023 by the authors. Licensee MDPI, Basel, Switzerland. This article is an open access article distributed under the terms and conditions of the Creative Commons Attribution (CC BY) license (https://creativecommons.org/licenses/by/4.0/).

1. Introduction

Atmospheric methane (CH_4) is the second most critical greenhouse gas responsible for ≈20% of the direct lower tropospheric warming caused by well-mixed greenhouse gases [1–3]. According to climate data records reconstructed from polar ice cores [4,5], the concentration of CH_4 in 2019 more than doubled since preindustrial times [6] (IPCC AR6 2021, A.2.1). CH_4 has a much shorter atmospheric lifetime (about one decade) than CO_2 (longer than one century), while each CH_4 molecule has a global warming potential of 84 and 28 times greater than CO_2 for time spans of 20 and 100 years, respectively [3,6–8]. CH_4

may have caused as much as half of the global temperature increase since preindustrial times [6]. It is therefore critical to monitor the global distribution of and changes in CH_4 and gain an understanding of the response and impact on the climate and environment [9–16].

Since current ground-based measurements are sparse, especially in remote land-based source regions, measurements from environmental satellites play an important role in assessing CH_4 concentrations by providing continuous spatiotemporal observations [17]. In the last two decades, a series of satellite passive sensors have been launched by international space agencies to provide observations of atmospheric CH_4 as well as other greenhouse gas (GHG) concentrations. Among these observing systems are the Scanning Imaging Absorption spectrometer for Atmospheric ChartographY (SCIAMACHY) onboard the European Space Agency (ESA) ENVISAT (2003–2012), which operates in the UV, visible, and near-infrared (near-IR) spectral regions [18], followed by the Thermal and Near-Infrared Sensor for Carbon Observation (TANSO) onboard the Japanese JAXA/NIES/MOE Greenhouse gases Observing Satellite (GOSAT), which has been in operation since 2009, along with GOSAT-2 starting in 2018 [19–21]. These NIR sensors were recently joined by the Tropospheric Monitoring Instrument (TROPOMI) onboard the Copernicus Sentinel-5 Precursor (S5P) satellite, launched in October 2017 [22], along with GHGSat, launched in June 2016 [23]. The CH_4 products derived from these NIR sensors measure a total column average from hyperspectral measurements of reflected NIR radiation scattered and absorbed by CH_4 with the spectra ranging from 1.6 to 2.3 μm, which includes a mixture of surface and column atmospheric source contributions. The applications of the NIR sensors have demonstrated capabilities of mapping the regional distribution and detecting point source anomalies. Other source imagers soon to be launched, such as MethaneSAT, GeoCarb, Carbon Mapper, etc., can also detect emissions from individual facilities [24].

In addition to these passive sensors and of specific interest to this work, the hyperspectral thermal infrared (TIR) sounders onboard the polar-orbiting satellites, such as the Atmospheric Infrared Sounder (AIRS) onboard the NASA Earth Observing System (EOS)/Aqua [25], the Cross-track Infrared Sounder (CrIS) onboard the Suomi National Polar-orbiting Partnership (SNPP) and NOAA-20 [26], as well as the Infrared Atmospheric Sounding Interferometer (IASI) operating on Metop satellites provided by Centre National d'Etudes Spatiales (CNES, France) [27], have also been used to derive CH_4 concentration. These hyperspectral sounders were originally designed for retrievals of the atmospheric temperature and moisture soundings; however, the channels near the 7.66 μm absorption band can be used to detect methane concentrations. Over the past two decades, global CH_4 environmental data records (EDRs) have been continuously generated by exploiting data from these hyperspectral TIR sensors. While the TIR sensors are not sensitive to the CH_4 in the lower troposphere near the surface (as described in Section 2), the continuous global data records produced from these sensors provide valuable information for monitoring CH_4 concentration in the middle troposphere. The currently operating and planned hyperspectral TIR sounders are listed in Table 1 [7].

Table 1. Hyperspectral TIR Sounders onboard LEO Environmental Satellites.

Satellite	Instruments (Providing Agency)	LEXT	Launch Dates
Aqua	AIRS (NASA)	01:30/13:30	2002
Metop-A,-B,-C	IASI (CNES)	09:30/21:30	2006, 2012, 2018
SNPP, JPSS-1,2,3,4	CrIS (NASA)	01:30/13:30	2011, 2017, 2022, 2027, 2032
Metop-SG-A1,2,3	IASI-NG (CNES)	09:30/21:30	2024, 2031, 2037

Several previous studies have been conducted to demonstrate uses of the hyperspectral TIR measurements for the evaluation of free tropospheric methane concentrations, for example, Xiong et al. [28] for AIRS, Razavi [29] for IASI, and Smith and Barnet [30] for CrIS. In this paper, we analyze the spatiotemporal global distributions, and long-term trends, especially the latitudinal and seasonality dependencies of CH_4 concentrations derived from the advanced hyperspectral sounders flown in the same 01:30/13:30 local equator crossing time (LEXT) orbits (i.e., CrIS and AIRS). To gain insight into the changes between the surface and upper tropospheric CH_4, the satellite retrievals from AIRS and CrIS are also compared with NOAA Global Monitoring Laboratory (GML) in situ observations and model outputs. The AIRS physical retrieval algorithm has been adapted at NOAA for application to the operational CrIS system (with ongoing updates and improvements). This has enabled the provision of consistent atmospheric vertical profile EDRs from 2002 to the present. The CrIS sensor is part of the technical baseline for the JPSS program satellites, so these hyperspectral TIR data and profile EDRs are expected to extend through the JPSS-4 timeframe into the 2040s.

This study's main objective is to understand the spatiotemporal global distributions and changes in atmospheric methane derived from the new generation of satellite hyperspectral TIR instruments (e.g., AIRS and CrIS). Section 2 describes the data sources and retrieval methodology. The global CH_4 distributions, the rate of changes, and the latitudinal variations derived from the satellite data are presented in Section 3. The results are discussed in Section 4, followed by conclusions in Section 5.

2. Methods

2.1. CrIS and AIRS Observations

The CrIS instruments are Fourier transform spectrometers, and their characteristics and channel information have been described in previous studies [31–36]. We use data spanning back to December 2014, when the SNPP CrIS instrument was operating in full spectral resolution at 0.625 cm^{-1} in all 3 bands and a total of 2211 channels [32]. AIRS is an IR grating spectrometer with 2378 discrete channels as described in studies [25,37,38]. AIRS has demonstrated an estimated stability of ~4 mK/year [39]. The radiometric stability of the AIRS radiances has been recently estimated to be better than 0.02 to 0.03 K per decade versus minor gas anomalies in the NOAA/GML in situ measurements in several AIRS channels, which are within the levels of climate trending, roughly on the order of 0.1 K per decade [40].

2.2. The AIRS and CrIS Retrieved CH_4 Profiles

The AIRS science team retrieval algorithm is described in Susskind et al. (2003) [41], including the sensor calibration, microwave (MW) first guess retrieval, cloud-clearing, initial first guess IR retrieval, and a final IR physical retrieval. The cloud-clearing step enables the use of partially cloudy measurements [42,43]. Validation and improvements of AIRS retrievals are described in Fetzer et al. [44], Tobin et al. [45], Divakarla et al. [46], Chahine et al. [38], Susskind et al. [47], Nalli et al. [48], and many other studies. Because of the AMSU-A2 instrument failure, AIRS products using both TIR and MW were discontinued after 24 September 2016. Thus, for a consistent data record, we use AIRS Version 7 IR-only retrievals for the entire record from the NASA Goddard Earth Sciences (GES) Data and Information Services Center (DISC) (https://disc.gsfc.nasa.gov, accessed on 4 June 2023) [49].

The NOAA Unique Combined Atmospheric Processing System (NUCAPS) is the NOAA operational retrieval algorithm for the operational hyperspectral thermal IR sounders [50]. The NUCAPS algorithm is based on the AIRS science team retrieval algorithm Version 5 [30,41,47] which differs primarily in the first guess methodology (v5 uses a linear eigenvector regression, whereas v7 uses a neural network nonlinear regression) [41]. The NUCAPS algorithm runs operationally at NOAA/NESDIS, with the operational products being publicly available from the Comprehensive Large Array-data Stewardship System (CLASS).

Both the AIRS and NUCAPS CrIS retrieval algorithms use spectral channels near 7.66 μm to retrieve CH_4 [28,29]. The CH_4 channel selection is based on the sensitivity to CH_4 as indicated by the kernel functions [51,52]. To reduce interference from other absorbing species, channels with overlapping absorption bands (e.g., water vapor and

HNO_3) are minimized. The AIRS and NUCAPS CH_4 retrievals are generally sensitive in the range between 650 hPa and the lower stratosphere, with peak sensitivity around 300–400 hPa, depending on surface and atmospheric conditions [53]. The CH_4 weighting function, or Jacobian matrix, describes the portion of the CH_4 profile represented by each radiance measurement [54,55]. An example of the CrIS CH_4 Jacobian matrix, calculated from the Standalone AIRS Radiative Transfer Algorithm (SARTA, see algorithm description in Strow et al., 2003), is shown in Figure 1. From Figure 1, it is clear that the most CH_4-sensitive region is the middle to upper troposphere (i.e., ~200–600 hPa), as depicted in the non-red color shades in Figure 1. The peak of the sensitivity can be higher or lower depending on the local scenario of CH_4 profiles.

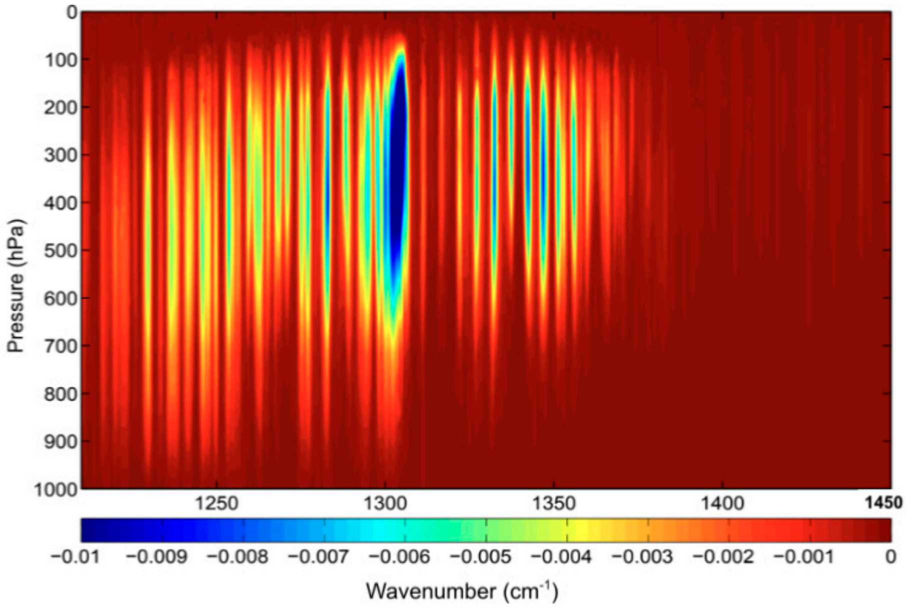

Figure 1. CH_4 Jacobians for CrIS based on an example atmospheric profile for 15°N latitude: the *x*-and *y*-axes show spectral wave numbers (cm^{-1}) and the vertical pressure coordinate (hPa), respectively.

Prior to the CH_4 retrieval step in the algorithm, the atmospheric vertical temperature and moisture profiles (AVTP and AVMP, respectively), surface skin temperatures, and land emissivity are retrieved using different channels than those used for CH_4 retrievals. These data, as well as the a priori profiles of CH_4, are used as inputs to SARTA forward calculation [56–58]. The difference between the observed and calculated radiances (obs minus calc) is minimized to construct an error covariance matrix, from which the change of CH_4 is derived using an eigenvector transformation and damping. The final retrieved profile of CH_4 is usually obtained through several iterations. For more details on the NUCAPS and AIRS algorithm, see Susskind et al. [41], the NUCAPS Algorithm Theoretical Basis Document (ATBD) (2021), and Smith and Barnet [30]; for the details of the CH_4 first guess and channel selections, see Warner et al. [51], Xiong et al. [28], and Gambacorta et al. [52].

The NUCAPS CH_4 retrieval has been significantly improved over the last 2 years. The major changes include updates of the CH_4 and N_2O a priori, quality control criteria, and refinements in the CH_4 channel selection. There were also other NUCAPS algorithm enhancements, such as the updated TIR spectral tuning (i.e., an empirical radiance bias correction), which improved the performance of the NUCAPS temperature and water vapor retrievals, which in turn had a positive impact on the downstream CH_4 products. The CH_4 retrievals from CrIS on SNPP and NOAA-20 have gone through a thorough validation process by comparative analysis using in situ data and similar products from other satellite sensors [59–62]. For the AIRS and CrIS CH_4 products, we estimated a precision of 1%. While the same retrieval approach was used for AIRS and NUCAPS algorithms, the differences in the sensors, channels, a priori, tuning, and quality control can contribute to the differences in CH_4 retrievals between AIRS and CrIS.

2.3. Rate of Change of CH_4 Concentrations

The global mean growth rate of CH_4 has been changing over the last three decades [63] (Dlugokencky et al. 2003). The global growth rate of CH_4 based on GML in situ measurements was 11.9 ± 0.9 ppb yr^{-1} from 1984 to 1989, declined from 1990 to 1998, and then reached nearly zero growth from 1999 to 2005 [13,64–68]. A renewed strong growth in global CH_4 began in 2006 [10,14,69]. Growth in global CH_4 has been accelerating recently, further increasing from 2015 to 2020 [9]. The annual CH_4 concentration increase in 2020 was 15.19 ± 0.41 ppb yr^{-1} (https://gml.noaa.gov/ccgg/trends_ch4/, accessed on 4 June 2023), which was the largest annual increase recorded since 1983 when NOAA/GML's ongoing measurements began [70].

We attempt to examine the same trends using global TIR satellite measurements spanning the last decades. We follow the fitting methods of Nisbet et al. (2016) [71] as shown below:

We fit a daily averaged CH_4 time series at each latitude with a 2nd-order polynomial and a number of periods of sine and cosine series,

$$y(t) = y_p(t) + y_s(t) + E(t) \tag{1}$$

where $t = \frac{doy-0.5}{Num\_days} + year - year0$ represents middle point in each day, here DOY states the day of the year, num_days is a total number of days in the year, year0 = 2000.0 is the starting year, $y_p(t)$ represents trend signal,

$$y_p(t) = p_0 + p_1 t + p_2 t^2 \tag{2}$$

and $y_s(t)$ represents seasonal signals,

$$y_s(t) = \sum_{k=1}^{4} [A_k sin(2\pi kt) + B_k cos(2\pi kt)] \tag{3}$$

k = 0.5, 1, 2, 3, 4, 6, 12, 24, and 52, which represents the 2-year, 1-year, 1/2-year, 1/3-year and 1/4-year periods, 2-month, 1-month, half-month, and weekly cycles. There are total of 21 fitting coefficients in each latitude. The table of coefficients was uploaded in two separate NetCDF files, for AIRS and CrIS, respectively, in the Supplementary Materials.

$E(t)$ represents the fitting residuals, which is filtered by a low pass filter, i.e., at roughly 2 years,

$$E(t) = E_{low}(t) + \varepsilon \tag{4}$$

where $E_{low}(t)$ denotes the signal passed by the low band filter, and ε is the high-frequency noise; y_p is paired with $E_{low}(t)$ to form the long-term trend of CH_4 monthly mean, that is

$$y_n(t) = y_p(t) + E_{low}(t) \tag{5}$$

Then the annual CH_4 rate at each day can be calculated

$$R(t) = \frac{dy_n(t)}{dt} = \frac{dy_p(t) + dE_{low}(t)}{dt} \tag{6}$$

2.4. CH_4 Ground Observation Network

NOAA GML has been recording CH_4 measurements since 1983 at a globally distributed network of in situ surface sampling sites [62]; the details and maps of the site locations are available on the public website: NOAA's Global Greenhouse Gas Reference Network, https://gml.noaa.gov/ccgg/about.html, accessed on 4 June 2023. The network was originally designed to sample the global "background" atmosphere far from strong local sources, and despite some increase in coverage over time, the network remains sparse in space and time. More recently, in situ profiles have been added using a network of light aircraft, communications towers, and balloon-borne samplers. These measurements are well characterized and provide invaluable information for global CH_4 monitoring [63]. GML profile observations from aircraft, balloon-borne, and AirCore have been used as the truth for the validation of the NUCAPS CH_4 profile retrievals [61]. In this study, we use the long-term GML in situ measurements in our analysis of TIR satellite CH_4 for comparison purposes. Because most GML data are collected at the surface or in the lower troposphere while TIR retrievals are mostly sensitive to the middle to upper troposphere, direct comparisons are not possible. Nevertheless, the interannual differences between the in situ and TIR satellite observations provide valuable insights into vertical contrasts due to transport.

3. Results

3.1. CH_4 Global Distributions

The CH_4 time series from nearly two decades (2003–2020) of AIRS v7 retrievals [12,58,64,65] were analyzed in this study. As described in previous Section 2.2, the AIRS methane retrievals are broadly sensitive in the range between 850 hPa and the lower stratosphere, with peak sensitivity around 300–400 hPa, depending on surface and atmospheric conditions. Figure 2 displays annual mean global maps of satellite-retrieved CH_4 at 400 hPa for 2003 (left panel) and 2020 (right panel). The maps show similar patterns of the global CH_4 distribution, such as higher concentrations over the northern hemisphere (NH), the large-scale transport of plumes from biomass burning over Africa and South America, and large industrial emissions over Asia. Global CH_4 concentrations significantly increased over this time period, with the annual average in 2003 at ~1754 parts per billion (ppb) and ~1839 ppb in 2020. The total increase during this period was approximately 85 ppb, which represents a ~4.8% increase. For the same time period (2003–2020), the annual average of CH_4 concentrations observed from the GML surface measurements is ~1777 ppb in 2003 and ~1879 ppb in 2020, which is roughly a 5.7% increase. The satellite CH_4 concentrations from TIR sounders, which represent a broad layer roughly spanning 200–400 hPa [62], are lower than the GML in situ measurements as expected due to the latter's proximity to the source regions. Note that while the recent versions of the AIRS algorithm (V7, and V6) have implemented improvements in methane retrievals over previous versions (V5 and earlier), there might still be artifacts in the retrievals due to uncertainties in surface emissivity (especially over land/snow/ice surfaces) and cloud contamination in the cloud-cleared radiances that affect the results presented in Figure 2. There are ongoing efforts to improve the AIRS retrieval algorithms [66].

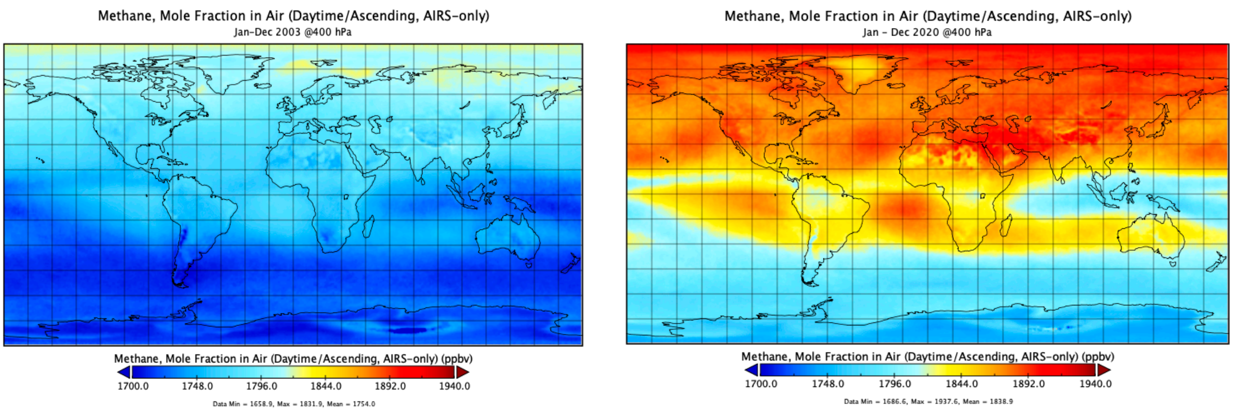

Figure 2. The annual mean of AIRS retrieved atmospheric CH_4 spanning a broad layer with an effective pressure of ≈400 hPa for the years 2003 (**left**) and 2020 (**right**), using the same color scale. (Data processed and downloaded from NASA GES Giovanni, and plotted with Panoply).

3.2. Rate of Change of CH_4 Concentrations from Satellite TIR Measurements

The evolution of CH_4 zonal distributions is shown in the upper panels of Figure 3, where the top left panel shows AIRS measurements and the top right panel shows the same measurements but with fitting, as described above. Whereas globally the CH_4 concentrations increased for all latitudes over time, stronger increases were observed in the NH in the earlier years, and beginning around 2008, the increases gradually expanded to the southern hemisphere (SH) and the Arctic region. The lower panels of Figure 3 show the rate of change calculated from the AIRS and CrIS TIR observations, where the bottom left and right are the deseasoned growth rates of AIRS and CrIS, respectively. The rate of change from AIRS also demonstrated the overall increase of CH_4 after 2008, especially the increases that have been expanding toward the SH and polar regions. The results from CrIS for 2015 to 2020 show general agreement with those from AIRS for the same period. Since it takes approximately one year for CH_4 to be mixed from the surface throughout the troposphere, the years with strong regional growth are usually followed by declines in the global background [72]. This pattern can be clearly seen from the early 2000s, but after 2014, the period of decline became less well defined and more dominant as seen by the overall positive increase rates. The satellite TIR results presented here are also generally consistent with those derived from in situ measurements [73].

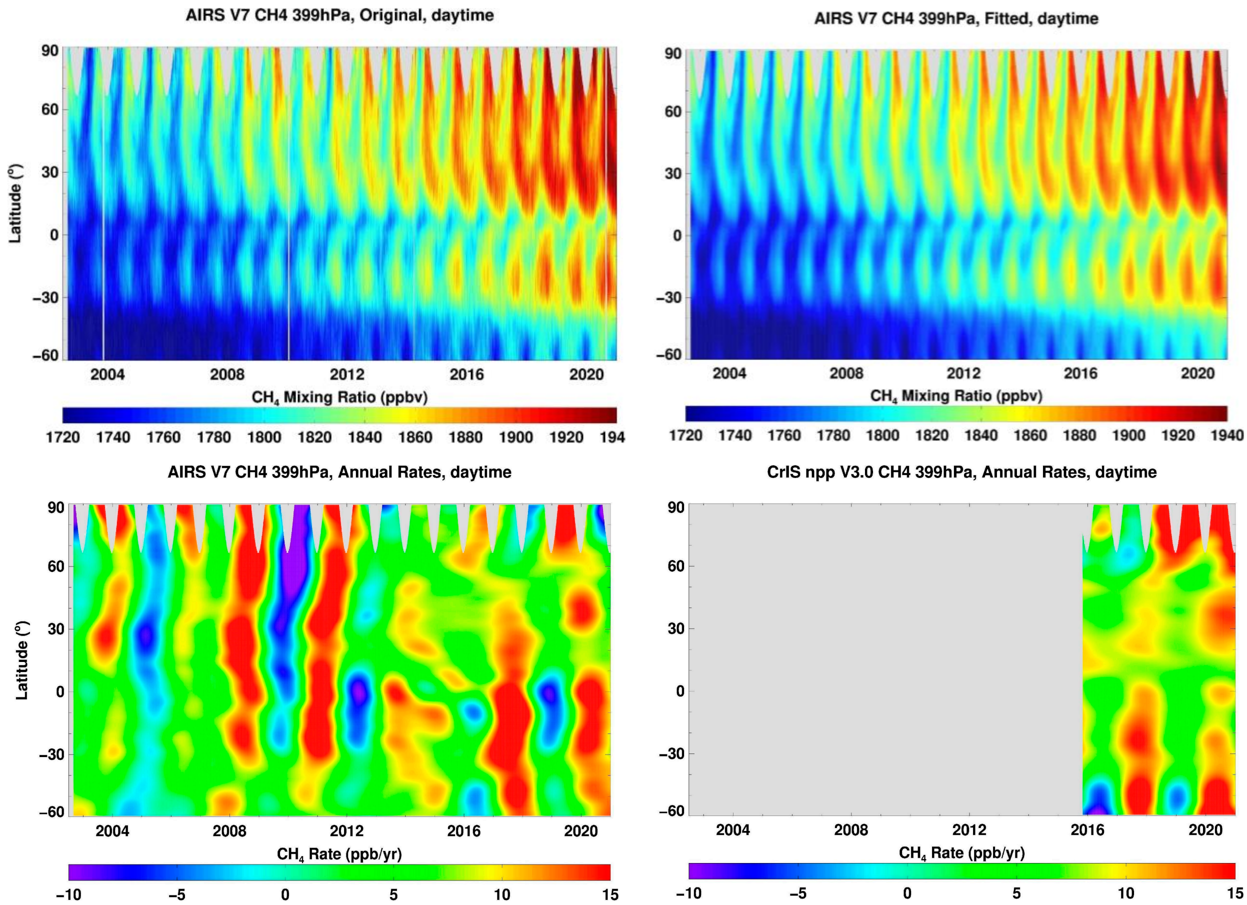

Figure 3. CH_4 zonal distributions with time (upper panel): AIRS raw (**upper left**), AIRS fitted (**upper right**), the corresponding rate of change from AIRS (**lower left**), and CrIS (**lower right**).

3.3. Interpolar CH_4 Difference

The zonal changes in CH_4 concentrations have been discussed in previous studies [9,70]. CH_4 concentrations are generally higher in the NH than the SH due to emission sources predominantly from NH land surfaces. The black curve in Figure 4 shows the averaged zonal mean variations from a 19-year average of AIRS CH_4 data at 400 hPa (2003–2021).

The lowest value (~1730 ppb, leftmost) is over the Antarctic region, and the highest value (~1858 ppb, rightmost) is over the Arctic region. The absolute CH_4 Interpolar Difference (IPD: the difference between zonal averages calculated for 60–90°N and 60–90°S) for the period is ~128 ppb. The zonal means from each year from 2003 to 2021 are also shown in Figure 4. The increase in the South Pole region is the smallest, compared with increases in the other latitudes. The two largest peaks of the increases in Figure 4 are in the north and south subtropical zones.

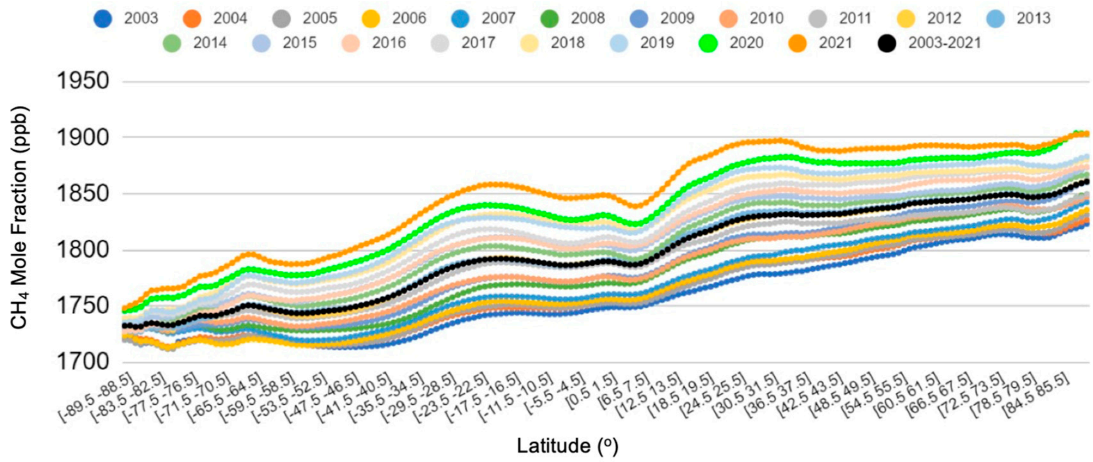

Figure 4. Zonal means of AIRS v7 tropospheric CH_4 near 400 hPa (in ppb) vertical level for each year from 2003 to 2021; the black line represents the averaged 19 years of AIRS data from 2003 to 2021.

3.4. Latitudinal Variations

To understand the latitudinal variation of TIR-derived CH_4, we examined the time series of CH_4 over different latitudinal zones retrieved from AIRS and CrIS and compared those with the GML in situ measurements. It is important to keep in mind that the TIR-based measurements represent a broad tropospheric layer roughly spanning 200–400 hPa. Figure 5 shows the CH_4 zonal mean time series (centered at 400 hPa) for latitude ranges of 60–90°N (top panel), 30–60°N (2nd panel), 0–30°N (3rd panel), 30°S–0 (4th panel), and 60–30°S (lowest panel) respectively. The CH_4 retrievals from AIRS (blue lines, 2003–2020) and CrIS (orange lines, 2015–2020) agree well with each other, both showing that the overall tropospheric CH_4 concentrations have been increasing across all latitudinal zones. The trends are similar to those of the GML in situ observations (green lines, 2003–2020), although the magnitudes of the CH_4 concentrations derived from each measurement approach can vary.

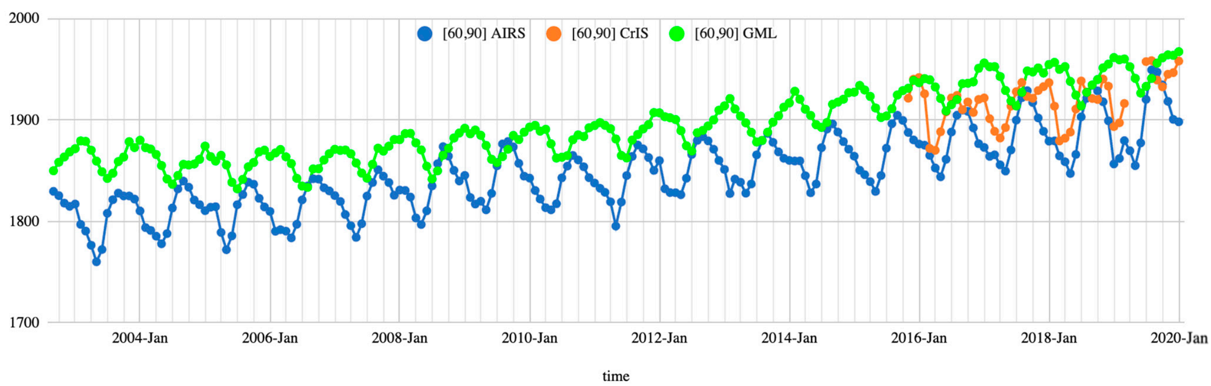

Figure 5. *Cont.*

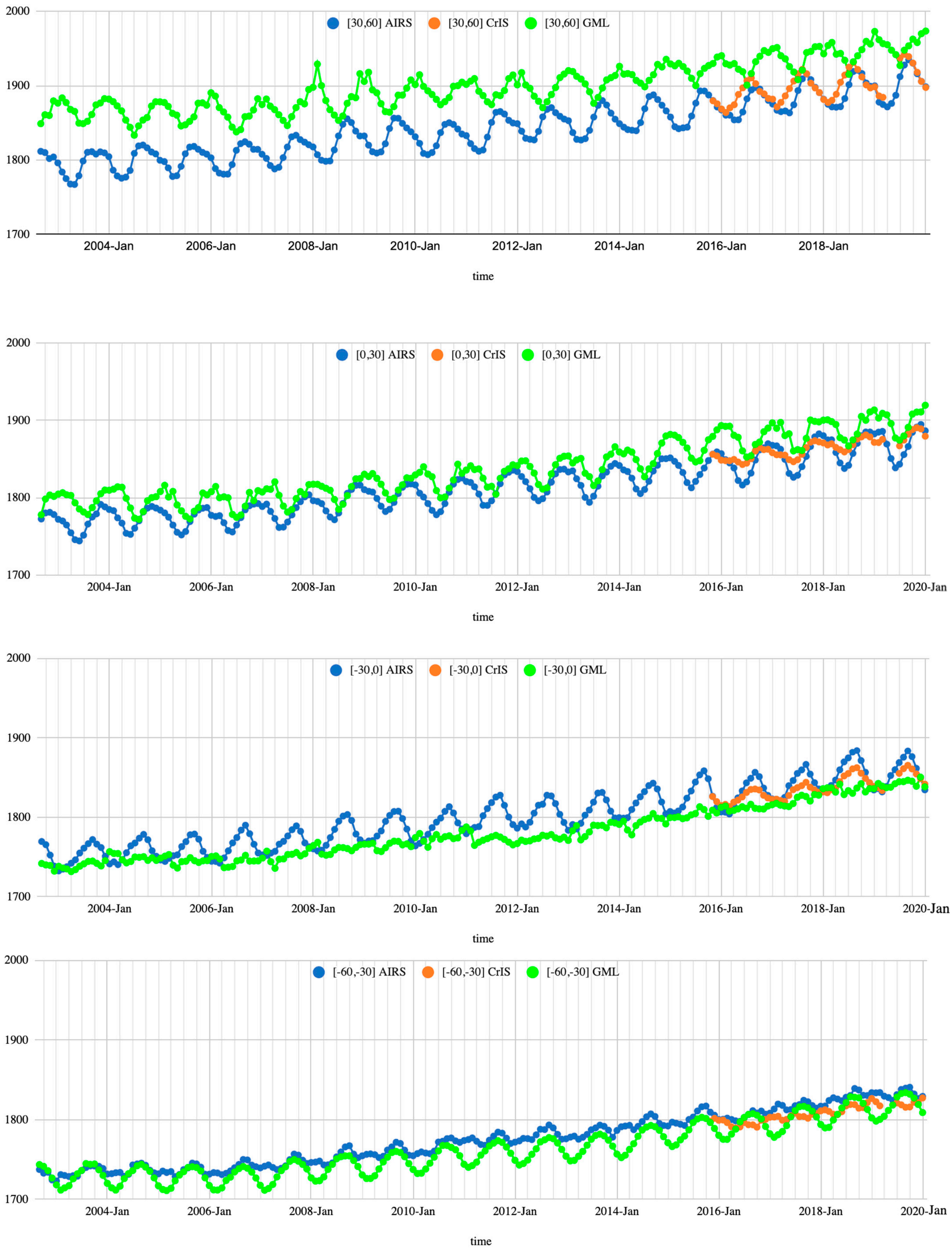

Figure 5. Time series of CH_4 (in ppb) retrieved from AIRS (blue), CrIS (orange) at 400 hPa, and in situ measurements from NOAA GML (green) for different latitudinal zones: 60–90°N (**top panel**); 30–60°N (**2nd panel**); 0–30°N (**3rd panel**); 0–30°S (**4th panel**); 30–60°S (**lowest panel**).

The CH_4 concentrations show annual cycles that vary at different latitudes. As seen in Figure 5, the amplitudes of the annual cycle are higher for the middle and high latitudes in the NH than they are in the tropics—this is primarily because the CH_4 sources are mostly located in the NH mid-to-high latitudes. Additionally, microbial sources (especially wetlands) can exhibit a strong seasonality, and more importantly, the seasonal cycles are controlled by chemistry. In fact, at the surface in the NH, the minimum occurs in summer when the microbial sources could be expected to be the strongest. Seasonal differences in transport also play a role. Figure 5 shows clearly that the TIR retrieved CH_4 from AIRS and CrIS has an overall negative bias than those from GML in the NH, which is consistent with CH_4 concentrations being higher in the boundary layer from source regions at the surface and decreasing in the free troposphere.

The in situ CH_4 measurements from GML are higher than AIRS CH_4 by 105 ppb at 60–90°N, 122 ppb at 30–60°N, and 56 ppb at 0–30°N, respectively. However, in the SH, the CH_4 retrievals at 400 hPa are higher than or close to those from the surface observations. On average, the AIRS CH_4 is 4 ppb higher than those from GML in the SH, and 0.5 ppb for CrIS.

Figure 5 also shows a prominent phase shift in the annual cycles of satellite TIR retrievals and the in situ measurements, especially in the mid-to-high NH latitudes. This phase shift is not obvious in the low latitudes in both the NH and SH. In the Arctic region (60 to 90°N), the tropospheric CH_4 concentrations retrieved from AIRS and CrIS show about 7–8 months of lag compared with the in situ concentrations. Similar phase shifts are observed in the NH middle latitudes (30–60°N), with lags of about 4–5 months. Such lags are minimal for the NH and SH tropics (30°S to 30°N).

The AIRS CH_4 in SH middle latitudes show two peaks in the seasonal cycles, one of which represents the same seasonal cycle as in GML in situ measurements, whereas the other peak shows a similar phase shift as in the NH middle latitude. The SH high latitudes are not shown due to noisy retrievals contaminated by the Southern Ocean clouds.

4. Discussion

To better understand the vertical phase shifts in CH_4 seasonality, we examined the results from CarbonTracker-CH_4 [74,75]. CarbonTracker-CH_4 is NOAA GML's global atmospheric inversion system for estimating emissions of atmospheric CH_4 by assimilating global in situ measurements [76]. Since the first version of CarbonTracker-CH_4 was published in 2014, we revised our inversion system by jointly assimilating measurements of CH_4 and the stable isotopic ratio of CH_4 (denoted $\delta^{13}C$-CH_4), incorporating spatially and temporally resolved source signature of $\delta^{13}C$-CH_4 and optimizing fluxes at a grid scale. The current CarbonTracker-CH_4 is based on the TM5-4DVAR inversion system [77]; it simulated optimized monthly global microbial, fossil, and pyrogenic emissions at $3 \times 2°$ horizontal resolution (longitude by latitude) from 1997 to 2021. Based on the optimized emissions, the mole fraction of atmospheric CH_4 is simulated at 3-h, $3 \times 2°$ horizontal resolution with 25 vertical hybrid sigma pressure levels. Since CarbonTracker-CH_4 assimilates CH_4 mole fraction from more than 330 in situ sites, the simulated CH_4 mole fractions of the surface layer match well with the surface in situ measurements.

The CH_4 time series for different vertical levels and latitudinal bands from the CarbonTracker-CH_4 model runs are shown in Figure 6. Seven pressure levels are plotted from 200 to 800 hPa at 100 hPa intervals for every 30° latitudinal band. Similar phase shifts to those seen by the satellite TIR measurements, described in Section 3.3, can also be seen in these model results. The seasonality of CarbonTracker-CH_4 results at 800 hPa (Dark blue in Figure 6) resembles the seasonality of GML in situ measurements (Green in Figure 5), and the seasonality of CarbonTracker-CH_4 at 300–400 hPa (Green and sky blue in Figure 6) resembles AIRS/CrIS seasonality at 400 hPa (Blue and Orange in Figure 5). The seasonality of CarbonTracker-CH4 at 200 hPa shows the influence of stratospheric chemistry (Figure 7). The seasonality of CarbonTracker-CH4 at 300–400 hPa is influenced by both tropospheric (500–800 hPa) and stratospheric chemistry (200 hPa). The magnitude of the vertical shifts in CH_4 seasonality likely depends on the age and transport processes of CH_4 for the different zonal bands. This result is consistent with other studies on TIR sounders (Xiong et al. 2013; Worden et al. 2015; Kulawik et al. 2021; Xiong et al. 2022) [78–81], as TIR sounders are sensitive to atmospheric CH_4 in the middle troposphere through the lower stratosphere (2 to 17 km). These studies used TIR sounders to quantify atmospheric CH_4 variations and uncertainties associated with the stratospheric intrusion and troposphere-stratosphere exchange.

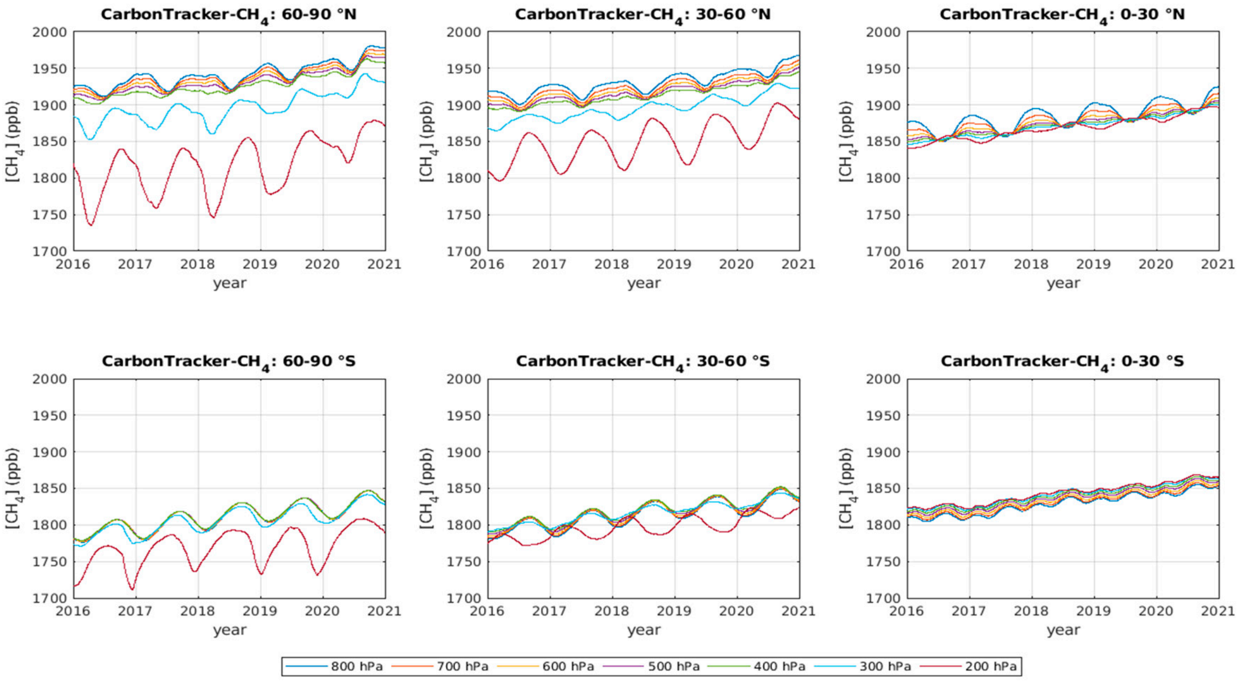

Figure 6. Time series of zonally averaged CH_4 from GML CarbonTracker-CH_4 from 2003 to 2020 at 200–800 hPa for different zonal bands: 60–90°N (**upper left**); 30–60°N (**upper middle**); 0–30°N (**upper right**); 90–60°S (**lower left**); 60–30°S (**lower middle**); and 30°S–0 (**lower right**).

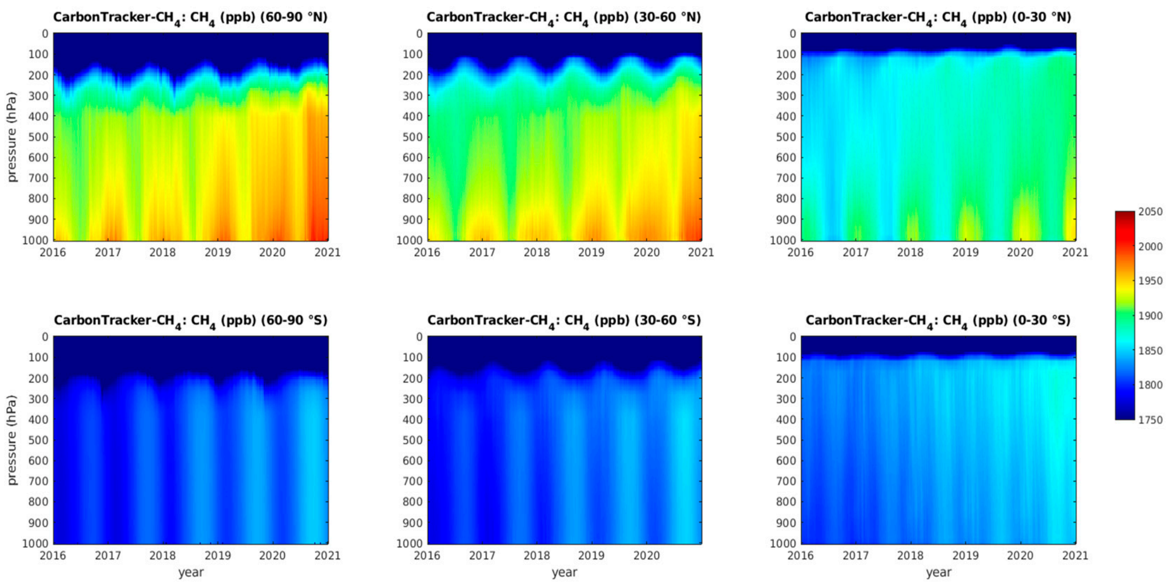

Figure 7. Pressure-altitude versus time cross sections of CH_4 from CarbonTracker-CH4 from 2003 to 2020 for different zonal bands: 60–90°N (**upper left**); 30–60°N (**upper middle**); 0–30°N (**upper right);** 90–60°S (**lower left**); 60–30°S (**lower middle**); and 30°S–0 (**lower right**).

The tropics (30°S to 30°N) show smaller vertical gradients than temperate and polar latitudinal bands due to strong convection from Hadley cells (Webster 2004) [82]. There are minimal phase shifts between the stratosphere and troposphere compared with the mid-to-high NH latitudes. For latitudes, 0–30°N, CarbonTracker-CH_4 at 300–400 hPa did not show a large seasonality (top-right plot in Figure 6), which is consistent with CrIS results. For latitude 0–30°S, there are two peaks throughout vertical layers, a larger peak in summer and a smaller peak in winter, consistent with GML's in situ measurements at Tutuila, American Samoa (bottom-right plot in Figure 6).

Figure 7 shows curtain plots of vertical cross sections of CH_4 over time for different global polar, mid-latitude, and tropical bands as discussed previously. Similar phase shifts are observed for the NH latitudes, and strong vertical gradients occur in the tropopause regions for NH mid-latitude and polar zones. In the SH, CH_4 concentrations remain almost constant throughout the troposphere. This may be attributed to the lack of emission sources in the SH. Figures 6 and 7 show that for the broad layer between 200 hPa and 400 hPa, where the TIR (AIRS and CrIS) retrievals are most sensitive, the retrievals may be influenced by stratospheric CH_4. The magnitude of the stratospheric influence varies with different latitude zones, depending on factors such as tropopause heights and deep convection. Specifically, in the NH mid- and high-latitude regions, stratospheric CH_4 seems to dominate the seasonality of retrieval results, whereas the SH mid-latitude information is a mix of tropospheric and stratospheric CH_4 information.

5. Conclusions

Hyperspectral thermal IR (TIR) sounders, such as AIRS and CrIS (as well as IASI), provide continuous long-term global data records of the mid-to-upper tropospheric CH_4. In this study, we analyzed spatial and temporal variations using AIRS and CrIS remote sensing measurements. Significant changes have been found for CH_4 concentrations at annual and interannual time scales, and at various latitudes. Increases in CH_4 concentrations and annual growth rates have also been studied. Our analyses showed strong increasing trends in the mid-to-upper troposphere from satellite measurements. There are latitudinal dependences for these increases, as well as seasonal dependencies.

We compared the TIR-retrieved broad-layer CH_4 concentrations with the GML global in situ observation network and discovered temporal phase shifts of the CH_4 seasonality between the two data sources. The phase shifts are most significant in the NH where the surface emissions are higher. We conclude that the CH_4 broad-layer concentrations from satellite TIR measurements are influenced by stratospheric contributions that represent different seasonality from the troposphere in the NH mid-to-high latitudes. This phase shift behavior is minimal in the low latitudes in both NH and SH; in the SH middle latitudes, the retrieved CH_4 information is influenced by both the troposphere and stratosphere. Additional analysis is needed to fully understand the seasonal phase differences between the surface and upper troposphere/lower stratosphere, which may include more in-depth model studies and high-altitude flight observations. Long-term annual to interannual trend studies are also important to comprehend global changes in CH_4 distributions. The CrIS sensors from NOAA-21 (launched successfully in November 2022), along with the planned low earth orbit (LEO) satellite missions will help to serve this goal.

Supplementary Materials: The following supporting information can be downloaded at: https://www.mdpi.com/article/10.3390/rs15122992/s1.

Author Contributions: Conceptualization, L.Z. and J.W.; Methodology, L.Z., J.W. and Z.W.; Formal analysis, L.Z. and J.W.; Investigation, L.Z., J.W., Y.O. and L.B.; Data curation, L.Z., J.W. and Z.W.; Writing—original draft, L.Z.; Writing—review & editing, J.W., N.R.N., Z.W., M.D., K.P., X.L., S.K. and M.D.G.; Visualization, L.Z.; Supervision, J.W. All authors have read and agreed to the published version of the manuscript.

Funding: This research is based on work funded by the NOAA JPSS Office, and contributions from the Global Monitoring Laboratory were supported by the NOAA OAR and NOAA JPSS.

Data Availability Statement: The data used is either in the links provided in the text or in the supplement materials.

Acknowledgments: This publication describes the collective work of government industry and academic teams over the course of many years. The authors would like to thank especially JPSS STAR NUCAPS team (current and previous team members), and NOAA GML teams for their contributions. The manuscript contents are solely the opinions of the authors and do not constitute a statement of policy, decision, or position on behalf of NOAA or the U.S. government. The authors also wish to acknowledge the availability of the in situ measurements provided by NOAA Global Monitoring Laboratory (GML), the AIRS version 7 level 2 CH_4 products from NASA Earthdata center (Data citation: AIRS project (2019), Aqua/AIRS L3 Monthly Standard Physical Retrieval (AIRS-only) 1 degree x 1 degree V7.0, Greenbelt, MD, USA, Goddard Earth Sciences Data and Information Services Center (GES DISC), Accessed 2 April 2022, https://doi.org/10.5067/UBENJB9D3T2H).

Conflicts of Interest: The authors declare no conflict of interest.

References

1. Ramanathan, V.; Cicerone, R.J.; Singh, H.B.; Kiehl, J.T. Trace gas trends and their potential role in climate change. *J. Geophys. Res. Atmos.* **1985**, *90*, 5547–5566. [CrossRef]
2. Houghton, J.T.; Ding, Y.; Griggs, D.J.; Noguer, M.; van der Linden, P.J.; Dai, X.; Maskell, K.; Johnson, C.A. (Eds.) IPCC (2001) Climate change: The scientific basis. In *Contribution of Working Group I to the Third Assessment Report of the Intergovernmental Panel on Climate Change*; Cambridge University Press: Cambridge, UK, 2001; p. 881.
3. Stocker, T.F.; Qin, D.; Plattner, G.-K.; Tignor, M.; Allen, S.K.; Boschung, J.; Nauels, A.; Xia, Y.; Bex, V.; Midgley, P.M. (Eds.) IPCC (2013). Climate Change 2013: The Physical Science Basis. In *Contribution of Working Group I to the Fifth Assessment Report of the Intergovernmental Panel on Climate Change*; Cambridge University Press: Cambridge, UK; New York, NY, USA, 1585.
4. Etheridge, D.M.; Steele, L.P.; Francey, R.J.; Langenfelds, R.L. Atmospheric methane between 1000 A.D. and present: Evidence of anthropogenic emissions and climatic variability. *J. Geophys. Res. Atmos.* **1998**, *103*, 15979–15993. [CrossRef]
5. Rubino, M.; Etheridge, D.M.; Thornton, D.P.; Howden, R.; Allison, C.E.; Francey, R.J.; Langenfelds, R.L.; Steele, L.P.; Trudinger, C.M.; Spencer, D.A.; et al. Revised Records of Atmospheric Trace Gases CO_2, CH_4, N_2O, and $\Delta_{13}C$-CO_2 over the Last 2000 years from Law Dome, Antarctica. *Earth Syst. Sci. Data* **2019**, *11*, 473–492. [CrossRef]
6. Masson-Delmotte, V.; Zhai, P.; Pirani, A.; Connors, S.L.; Péan, C.; Berger, S.; Caud, N.; Chen, Y.; Goldfarb, L.; Gomis, M.I. (Eds.) IPCC 2021: Climate Change 2021: The Physical Science Basis. In *Contribution of Working Group I to the Sixth Assessment Report of the Intergovernmental Panel on Climate Change*; Cambridge University Press: Cambridge, UK, 2021.
7. Crisp, D.; Meijer, Y.; Munro, R.; Bowman, K.; Chatterjee, A. *A Constellation Architecture for Monitoring Carbon Dioxide and Methane from Space*; CEOS: New York, NY, USA, 2018.
8. Voulgarakis, A.; Naik, V.; Lamarque, J.-F.; Shindell, D.T.; Young, P.J.; Prather, M.J.; Wild, O.; Field, R.D.; Bergmann, D.; Cameron-Smith, P.; et al. Analysis of present day and future OH and methane lifetime in the ACCMIP simulations. *Atmos. Meas. Tech.* **2013**, *13*, 2563–2587. [CrossRef]
9. Nisbet, E.G.; Manning, M.R.; Dlugokencky, E.J.; Fisher, R.E.; Lowry, D.; Michel, S.E.; Myhre, C.L.; Platt, S.M.; Allen, G.; Bousquet, P.; et al. Very Strong Atmospheric Methane Growth in the 4 Years 2014–2017: Implications for the Paris Agreement. *Glob. Biogeochem. Cycles* **2019**, *33*, 318–342. [CrossRef]
10. Nisbet, E.G.; Fisher, R.E.; Lowry, D.; France, J.L.; Allen, G.; Bakkaloglu, S.; Broderick, T.J.; Cain, M.; Coleman, M.; Fernandez, J.; et al. Methane Mitigation: Methods to Reduce Emissions, on the Path to the Paris Agreement. *Rev. Geophys.* **2020**, *58*, e2019RG000675. [CrossRef]
11. Fung, I.; John, J.G.; Lerner, J.; Matthews, E.; Prather, M.; Steele, L.P.; Fraser, P.J. Three-dimensional model synthesis of the global methane cycle. *J. Geophys. Res. Atmos.* **1991**, *96*, 13033–13065. [CrossRef]
12. Worden, J.; Kulawik, S.; Frankenberg, C.; Payne, V.; Bowman, K.; Cady-Peirara, K.; Wecht, K.; Lee, J.-E.; Noone, D. Profiles of CH_4, HDO, H_2O, and N_2O with improved lower tropospheric vertical resolution from Aura TES radiances. *Atmos. Meas. Tech.* **2012**, *5*, 397–411. [CrossRef]
13. Dlugokencky, E.J.; Bruhwiler, L.; White, J.W.C.; Emmons, L.K.; Novelli, P.C.; Montzka, S.A.; Masarie, K.A.; Lang, P.M.; Crotwell, A.M.; Miller, J.B.; et al. Observational constraints on recent increases in the atmospheric CH_4 burden. *Geophys. Res. Lett.* **2009**, *36*. [CrossRef]
14. Nisbet, E.G.; Dlugokencky, E.J.; Bousquet, P. Atmospheric Science. Methane on the Rise—Again. *Science* **2014**, *343*, 493–495. [CrossRef]
15. Saunois, M.; Stavert, A.R.; Poulter, B.; Bousquet, P.; Canadell, J.G.; Jackson, R.B.; Raymond, P.A.; Dlugokencky, E.J.; Houweling, S.; Patra, P.K.; et al. The Global Methane Budget 2000–2017. *Earth Syst. Sci. Data* **2020**, *12*, 1561–1623. [CrossRef]
16. Kirschke, S.; Bousquet, P.; Ciais, P.; Saunois, M.; Canadell, J.G.; Dlugokencky, E.J.; Bergamaschi, P.; Bergmann, D.; Blake, D.R.; Bruhwiler, L.; et al. Three Decades of Global Methane Sources and Sinks. *Nat. Geosci.* **2013**, *6*, 813–823. [CrossRef]

17. Jacob, D.J.; Turner, A.J.; Maasakkers, J.D.; Sheng, J.; Sun, K.; Liu, X.; Chance, K.; Aben, I.; McKeever, J.; Frankenberg, C. Satellite observations of atmospheric methane and their value for quantifying methane emissions. *Atmos. Meas. Tech.* **2016**, *16*, 14371–14396. [CrossRef]
18. Frankenberg, C.; Aben, I.; Bergamaschi, P.; Dlugokencky, E.J.; van Hees, R.; Houweling, S.; van der Meer, P.; Snel, R.; Tol, P. Global column-averaged methane mixing ratios from 2003 to 2009 as derived from SCIAMACHY: Trends and variability. *J. Geophys. Res. Atmos.* **2011**, *116*. [CrossRef]
19. Yokota, T.; Yoshida, Y.; Eguchi, N.; Ota, Y.; Tanaka, T.; Watanabe, H.; Maksyutov, S. Global Concentrations of CO_2 and CH_4 Retrieved from GOSAT: First Preliminary Results. *Sola* **2009**, *5*, 160–163. [CrossRef]
20. Schepers, D.; Guerlet, S.; Butz, A.; Landgraf, J.; Frankenberg, C.; Hasekamp, O.; Blavier, J.-F.; Deutscher, N.M.; Griffith, D.W.T.; Hase, F.; et al. Methane retrievals from Greenhouse Gases Observing Satellite (GOSAT) shortwave infrared measurements: Performance comparison of proxy and physics retrieval algorithms. *J. Geophys. Res. Atmos.* **2012**, *117*. [CrossRef]
21. Saitoh, N.; Touno, M.; Hayashida, S.; Imasu, R.; Shiomi, K.; Yokota, T.; Yoshida, Y.; Machida, T.; Matsueda, H.; Sawa, Y. Comparisons between XCH4 from GOSAT Shortwave and Thermal Infrared Spectra and Aircraft CH4 Measurements over Guam. *Sola* **2012**, *8*, 145–149. [CrossRef]
22. Lorente, A.; Borsdorff, T.; Butz, A.; Hasekamp, O.; de Brugh, J.A.; Schneider, A.; Wu, L.; Hase, F.; Kivi, R.; Wunch, D.; et al. Methane retrieved from TROPOMI: Improvement of the data product and validation of the first 2 years of measurements. *Atmos. Meas. Tech.* **2021**, *14*, 665–684. [CrossRef]
23. Varon, D.J.; McKeever, J.; Jervis, D.; Maasakkers, J.D.; Pandey, S.; Houweling, S.; Aben, I.; Scarpelli, T.; Jacob, D.J. Satellite Discovery of Anomalously Large Methane Point Sources From Oil/Gas Production. *Geophys. Res. Lett.* **2019**, *46*, 13507–13516. [CrossRef]
24. Pandey, S.; Gautam, R.; Houweling, S.; van der Gon, H.D.; Sadavarte, P.; Borsdorff, T.; Hasekamp, O.; Landgraf, J.; Tol, P.; van Kempen, T.; et al. Satellite observations reveal extreme methane leakage from a natural gas well blowout. *Proc. Natl. Acad. Sci. USA* **2019**, *116*, 26376–26381. [CrossRef]
25. Aumann, H.H.; Chahine, M.T.; Gautier, C.; Goldberg, M.D.; Kalnay, E.; McMillin, L.M.; Revercomb, H.; Rosenkranz, P.W.; Smith, W.L.; Staelin, D.H.; et al. AIRS/AMSU/HSB on the Aqua Mission: Design, Science Objectives, Data Products, and Processing Systems. *IEEE Trans. Geosci. Remote Sens.* **2003**, *41*, 253–264. [CrossRef]
26. Goldberg, M.D.; Kilcoyne, H.; Cikanek, H.; Mehta, A. Joint Polar Satellite System: The United States next generation civilian polar-orbiting environmental satellite system. *J. Geophys. Res. Atmos.* **2013**, *118*, 13463–13475. [CrossRef]
27. Hilton, F.; Armante, R.; August, T.; Barnet, C.; Bouchard, A.; Camy-Peyret, C.; Capelle, V.; Clarisse, L.; Clerbaux, C.; Coheur, P.-F.; et al. Hyperspectral Earth Observation from IASI: Five Years of Accomplishments. *Bull. Am. Meteorol. Soc.* **2012**, *93*, 347–370. [CrossRef]
28. Xiong, X.; Barnet, C.; Maddy, E.; Sweeney, C.; Liu, X.; Zhou, L.; Goldberg, M. Characterization and validation of methane products from the Atmospheric Infrared Sounder (AIRS). *J. Geophys. Res. Atmos.* **2008**, *113*. [CrossRef]
29. Razavi, A.; Karagulian, F.; Clarisse, L.; Hurtmans, D.; Coheur, P.F.; Clerbaux, C.; Müller, J.F.; Stavrakou, T. Global distributions of methanol and formic acid retrieved for the first time from the IASI/MetOp thermal infrared sounder. *Atmos. Meas. Tech.* **2011**, *11*, 857–872. [CrossRef]
30. Smith, N.; Barnet, C.D. Uncertainty Characterization and Propagation in the Community Long-Term Infrared Microwave Combined Atmospheric Product System (CLIMCAPS). *Remote Sens.* **2019**, *11*, 1227. [CrossRef]
31. Thomas, F.L.; Nelson, C.S.; Dills, P.; Riishojgaard, L.P.; Jones, A.; Li, L.; Miller, S.; Flynn, L.E.; Jedlovec, G.; McCarty, W.; et al. NPOESS. *Bull. Am. Meteorol. Soc.* **2009**, *91*, 727–740.
32. Zou, C.-Z.; Zhou, L.; Lin, L.; Sun, N.; Chen, Y.; Flynn, L.E.; Zhang, B.; Cao, C.; Iturbide-Sanchez, F.; Beck, T.; et al. The Reprocessed Suomi SNPP Satellite Observations. *Remote Sens.* **2020**, *12*, 2891. [CrossRef]
33. Han, Y.; Revercomb, H.; Cromp, M.; Gu, D.; Johnson, D.; Mooney, D.; Scott, D.; Strow, L.; Bingham, G.; Borg, L.; et al. Suomi Npp Cris Measurements, Sensor Data Record Algorithm, Calibration and Validation Activities, and Record Data Quality. *J. Geophys. Res. Atmos.* **2013**, *118*, 12734–12748. [CrossRef]
34. Han, Y.; Chen, Y. Calibration Algorithm for Cross-Track Infrared Sounder Full Spectral Resolution Measurements. *IEEE Trans. Geosci. Remote Sens.* **2017**, *56*, 1008–1016. [CrossRef]
35. Sanchez, F.; Tobin, D.S.; Scott, D.; Mooney, D.; Johnson, D.; Suwinski, L.; Predina, J.; Bolen, D.; Guenther, B.; Yan, B. NOAA-20 Cris Sdr Report for Validated Maturity Review. NOAA JPSS Science Review. 2018. Available online: https://www.star.nesdis.noaa.gov/jpss/documents/AMM/N20/CrIS_SDR_Validated.pdf (accessed on 17 March 2021).
36. Yan, B.; Goldberg, M.; Jin, X.; Liang, D.; Huang, J.; Porter, W.; Sun, N.; Zhou, L.; Pan, C.; Iturbide-Sanchez, F.; et al. A New 32-Day Average-Difference Method for Calculating Inter-Sensor Calibration Radiometric Biases between SNPP and NOAA-20 Instruments within ICVS Framework. *Remote Sens.* **2021**, *13*, 3079. [CrossRef]
37. Pagano, T.; Aumann, H.; Hagan, D.; Overoye, K. Prelaunch and in-flight radiometric calibration of the atmospheric infrared sounder (AIRS). *IEEE Trans. Geosci. Remote Sens.* **2003**, *41*, 265–273. [CrossRef]
38. Chahine, M.T.; Pagano, T.S.; Aumann, H.H.; Atlas, R.; Barnet, C.; Blaisdell, J.; Chen, L.; Divakarla, M.; Fetzer, E.J.; Goldberg, M.; et al. AIRS. *Bull. Am. Meteorol. Soc.* **2006**, *87*, 911–926. [CrossRef]
39. Aumann, H.H.; Pagano, T.S. Using AIRS and IASI Data to Evaluate Absolute Radiometric Accuracy and Stability for Climate Applications. *Proc. SPIE* **2008**, 708504. [CrossRef]

40. Strow, L.L.; DeSouza-Machado, S. Establishment of AIRS climate-level radiometric stability using radiance anomaly retrievals of minor gases and sea surface temperature. *Atmos. Meas. Tech.* **2020**, *13*, 4619–4644. [CrossRef]
41. Susskind, J.; Barnet, C.D.; Blaisdell, J.M. Retrieval of atmospheric and surface parameters from AIRS/AMSU/HSB data in the presence of clouds. *IEEE Trans. Geosci. Remote Sens.* **2003**, *41*, 390–409. [CrossRef]
42. Smith, W.L. An improved method for calculating tropospheric temperature and moisture from satellite radiometer measurements. *Mon. Weather Rev.* **1968**, *96*, 387–396. [CrossRef]
43. Chahine, M.T. Remote Sounding of Cloudy Atmospheres. I. The Single Cloud Layer. *J. Atmos. Sci.* **1974**, *31*, 233–243. [CrossRef]
44. Fetzer, E.; McMillin, L.M.; Tobin, D.; Aumann, H.H.; Gunson, M.R.; McMillan, W.W.; Hagan, D.E.; Hofstadter, M.D.; Yoe, J.; Whiteman, D.N.; et al. AIRS/AMSU/HSB Validation. *IEEE Trans. Geosci. Remote Sens.* **2003**, *41*, 418–431. [CrossRef]
45. Tobin, D.C.; Revercomb, H.E.; Knuteson, R.O.; Lesht, B.; Strow, L.L.; Hannon, S.E.; Feltz, W.F.; Moy, L.A.; Fetzer, E.J.; Cress, T.S. Atmospheric Radiation Measurement site atmospheric state best estimates for Atmospheric Infrared Sounder temperature and water vapor retrieval validation. *J. Geophys. Res. Atmos.* **2006**, *111*. [CrossRef]
46. Divakarla, M.G.; Barnet, C.D.; Goldberg, M.D.; McMillin, L.M.; Maddy, E.; Wolf, W.; Zhou, L.; Liu, X. Validation of Atmospheric Infrared Sounder temperature and water vapor retrievals with matched radiosonde measurements and forecasts. *J. Geophys. Res. Atmos.* **2006**, *111*. [CrossRef]
47. Susskind, J.; Blaisdell, J.M.; Iredell, L.; Keita, F. Improved Temperature Sounding and Quality Control Methodology Using AIRS/AMSU Data: The AIRS Science Team Version 5 Retrieval Algorithm. *IEEE Trans. Geosci. Remote Sens.* **2010**, *49*, 883–907. [CrossRef]
48. Nalli, N.R.; Clemente-Colón, P.; Minnett, P.J.; Szczodrak, M.; Morris, V.; Joseph, E.; Goldberg, M.D.; Barnet, C.D.; Wolf, W.; Jessup, A.; et al. Ship-based measurements for infrared sensor validation during Aerosol and Ocean Science Expedition 2004. *J. Geophys. Res. Atmos.* **2006**, *111*. [CrossRef]
49. Yue, Q.; Lambrigtsen, B. *Airs Version 7 Level 2 Performance Test and Validation Report*; Jet Propulsion Laboratory, California Institute of Technology: Pasadena, CA, USA, 2020.
50. Kalluri, S.; Barnet, C.; Divakarla, M.; Esmaili, R.; Nalli, N.; Pryor, K.; Reale, T.; Smith, N.; Tan, C.; Wang, T.; et al. Validation and Utility of Satellite Retrievals of Atmospheric Profiles in Detecting and Monitoring Significant Weather Events. *Bull. Am. Meteorol. Soc.* **2022**, *103*, E570–E590. [CrossRef]
51. Warner, X.J. *Operational Trace Gas Products Algorithms and Quality Evaluation in NOAA Unique CrIS/ATMS Processing Systems*; NOAA: Washington, DC, USA, 2023; *in preparation*.
52. Gambacorta, A.; Barnet, C. Methodology and Information Content of the NOAA NESDIS Operational Channel Selection for the Cross-Track Infrared Sounder (CrIS). *IEEE Trans. Geosci. Remote Sens.* **2013**, *51*, 3207–3216. [CrossRef]
53. Gambacorta, A.; Barnet, C.; Wolf, W.; King, T.; Maddy, E.; Strow, L.; Xiong, X.; Nalli, N.; Goldberg, M. An Experiment Using High Spectral Resolution CrIS Measurements for Atmospheric Trace Gases: Carbon Monoxide Retrieval Impact Study. *IEEE Geosci. Remote Sens. Lett.* **2014**, *11*, 1639–1643. [CrossRef]
54. Rodgers, C.D. Retrieval of atmospheric temperature and composition from remote measurements of thermal radiation. *Rev. Geophys.* **1976**, *14*, 609–624. [CrossRef]
55. Rodgers, C.D. Characterization and error analysis of profiles retrieved from remote sounding measurements. *J. Geophys. Res. Atmos.* **1990**, *95*, 5587–5595. [CrossRef]
56. Conrath, B.J. Vertical Resolution of Temperature Profiles Obtained from Remote Radiation Measurements. *J. Atmos. Sci.* **1972**, *29*, 1262–1271. [CrossRef]
57. Maddy, E.S.; Barnet, C.D. Vertical Resolution Estimates in Version 5 of AIRS Operational Retrievals. *IEEE Trans. Geosci. Remote Sens.* **2008**, *46*, 2375–2384. [CrossRef]
58. Strow, L.L.; Hannon, S.E.; De Souza-Machado, S.; Motteler, H.E.; Tobin, D. An Overview of the AIRS Radiative Transfer Model. *IEEE Trans. Geosci. Remote Sens.* **2003**, *41*, 303–313. [CrossRef]
59. Susskind, J.; Blaisdell, J.M.; Iredell, L. Improved methodology for surface and atmospheric soundings, error estimates, and quality control procedures: The atmospheric infrared sounder science team version-6 retrieval algorithm. *J. Appl. Remote Sens.* **2014**, *8*, 084994. [CrossRef]
60. Zhou, L.; Divakarla, M.; Liu, X. An Overview of the Joint Polar Satellite System (JPSS) Science Data Product Calibration and Validation. *Remote Sens.* **2016**, *8*, 139. [CrossRef]
61. Nalli, N.R.; Barnet, C.D.; Reale, A.; Tobin, D.; Gambacorta, A.; Maddy, E.S.; Joseph, E.; Sun, B.; Borg, L.; Mollner, A.K.; et al. Validation of satellite sounder environmental data records: Application to the Cross-track Infrared Microwave Sounder Suite. *J. Geophys. Res. Atmos.* **2013**, *118*, 13628–13643. [CrossRef]
62. Nalli, N.R.; Tan, C.; Warner, J.; Divakarla, M.; Gambacorta, A.; Wilson, M.; Zhu, T.; Wang, T.; Wei, Z.; Pryor, K.; et al. Validation of Carbon Trace Gas Profile Retrievals from the NOAA-Unique Combined Atmospheric Processing System for the Cross-Track Infrared Sounder. *Remote Sens.* **2020**, *12*, 3245. [CrossRef]
63. Dlugokencky, E.J.; Steele, L.P.; Lang, P.M.; Masarie, K.A. The growth rate and distribution of atmospheric methane. *J. Geophys. Res. Atmos.* **1994**, *99*, 17021–17043. [CrossRef]
64. WMO Gas Station Report 2020-WMO Global Atmosphere Watch (GAW) World Data Center for Greenhouse Gas (WDCGG) Data Summary No 43, March 2020. Available online: https://gaw.kishou.go.jp/static/publications/summary/sum43/sum43.pdf (accessed on 4 June 2023).

65. Kahn, B.H.; Irion, F.W.; Dang, V.T.; Manning, E.M.; Nasiri, S.L.; Naud, C.M.; Blaisdell, J.M.; Schreier, M.M.; Yue, Q.; Bowman, K.W.; et al. The Atmospheric Infrared Sounder version 6 cloud products. *Atmos. Meas. Tech.* **2014**, *14*, 399–426. [CrossRef]
66. Thrastarson, H.T. (Ed.) AIRS/AMSU/HSB Version 7 Level 2 Product User Guide. 2021. Available online: https://docserver.gesdisc.eosdis.nasa.gov/public/project/AIRS/V7_L2_Product_User_Guide.pdf (accessed on 4 June 2023).
67. Ding, F.; Savtchenko, A.; Hearty, T.; Wei, J.; Theobald, M.; Vollmer, B.; Tian, B.; Fetzer, E. Assessing the Impacts of Two Averaging Methods on AIRS Level 3 Monthly Products and Multiyear Monthly Means. *J. Atmos. Ocean. Technol.* **2020**, *37*, 1027–1050. [CrossRef]
68. Dlugokencky, E.J.; Houweling, S.; Bruhwiler, L.; Masarie, K.A.; Lang, P.M.; Miller, J.B.; Tans, P.P. Atmospheric Methane Levels Off: Temporary Pause or a New Steady-State? *Geophys. Res. Lett.* **2003**, *30*. [CrossRef]
69. Steele, L.P.; Dlugokencky, E.J.; Lang, P.M.; Tans, P.P.; Martin, R.C.; Masarie, K.A. Slowing down of the global accumulation of atmospheric methane during the 1980s. *Nature* **1992**, *358*, 313–316. [CrossRef]
70. Chandra, N.; Patra, P.K.; Bisht, J.S.H.; Ito, A.; Umezawa, T.; Saigusa, N.; Morimoto, S.; Aoki, S.; Janssens-Maenhout, G.; Fujita, R.; et al. Emissions from the Oil and Gas Sectors, Coal Mining and Ruminant Farming Drive Methane Growth over the Past Three Decades. *J. Meteorol. Soc. Jpn. Ser. II* **2021**, *99*, 309–337. [CrossRef]
71. Nisbet, E.G.; Dlugokencky, E.J.; Manning, M.R.; Lowry, D.; Fisher, R.E.; France, J.L.; Michel, S.E.; Miller, J.B.; White, J.W.C.; Vaughn, B.; et al. Rising atmospheric methane: 2007–2014 growth and isotopic shift. *Glob. Biogeochem. Cycles* **2016**, *30*, 1356–1370. [CrossRef]
72. Butler, J.H.; Stephen, A. Montzka NOAA Annual Greenhouse Gas Index (AGGI). 2021. Available online: https://gml.noaa.gov/aggi/aggi.html (accessed on 4 June 2023).
73. Lan, X.; Nisbet, E.G.; Dlugokencky, E.J.; Michel, S.E. What do we know about the global methane budget? Results from four decades of atmospheric CH_4 observations and the way forward. *Philos. Trans. R. Soc. A Math. Phys. Eng. Sci.* **2021**, *379*, 20200440. [CrossRef] [PubMed]
74. Basu, S.; Lan, X.; Dlugokencky, E.; Michel, S.; Schwietzke, S.; Miller, J.B.; Bruhwiler, L.; Oh, Y.; Tans, P.P.; Apadula, F.; et al. Estimating emissions of methane consistent with atmospheric measurements of methane and $\delta^{13}C$ of methane. *Atmos. Meas. Tech.* **2022**, *22*, 15351–15377. [CrossRef]
75. Bruhwiler, L.; Dlugokencky, E.; Masarie, K.; Ishizawa, M.; Andrews, A.; Miller, J.; Sweeney, C.; Tans, P.; Worthy, D. CarbonTracker-CH4: An assimilation system for estimating emissions of atmospheric methane. *Atmos. Chem. Phys.* **2014**, *14*, 8269–8293. [CrossRef]
76. Lan, X.; Thoning, K.W.; Dlugokencky, E.J. Trends in globally-averaged CH4, N2O, and SF6 determined from NOAA Global Monitoring Laboratory measurements. Version 2023-02. *Trends Greenh. Gases* **2023**. [CrossRef]
77. Bousserez, N.; Henze, D.K.; Perkins, A.; Bowman, K.W.; Lee, M.; Liu, J.; Deng, F.; Jones, D.B.A. Improved analysis-error covariance matrix for high-dimensional variational inversions: Application to source estimation using a 3D atmospheric transport model. *Q. J. R. Meteorol. Soc.* **2015**, *141*, 1906–1921. [CrossRef]
78. Xiong, X.; Barnet, C.; Maddy, E.; Wofsy, S.; Chen, L.; Karion, A.; Sweeney, C. Detection of methane depletion associated with stratospheric intrusion by atmospheric infrared sounder (AIRS). *Geophys. Res. Lett.* **2013**, *40*, 2455–2459. [CrossRef]
79. Worden, J.R.; Turner, A.J.; Bloom, A.; Kulawik, S.S.; Liu, J.; Lee, M.; Weidner, R.; Bowman, K.; Frankenberg, C.; Parker, R.; et al. Quantifying lower tropospheric methane concentrations using GOSAT near-IR and TES thermal IR measurements. *Atmos. Meas. Tech.* **2015**, *8*, 3433–3445. [CrossRef]
80. Kulawik, S.S.; Worden, J.R.; Payne, V.H.; Fu, D.; Wofsy, S.C.; McKain, K.; Sweeney, C.; Daube Jr, B.C.; Lipton, A.; Polonsky, I.; et al. Evaluation of single-footprint AIRS CH_4 profile retrieval uncertainties using aircraft profile measurements. *Atmos. Meas. Tech.* **2021**, *14*, 335–354. [CrossRef]
81. Xiong, X.; Liu, X.; Wu, W.; Knowland, K.E.; Yang, Q.; Welsh, J.; Zhou, D.K. Satellite observation of stratospheric intrusions and ozone transport using CrIS on SNPP. *Atmos. Environ.* **2022**, *273*, 118956. [CrossRef]
82. Webster, P.J. The Elementary Hadley Circulation. *Hadley Circ. Present Past Future* **2004**, *21*, 9–60. [CrossRef]

Disclaimer/Publisher's Note: The statements, opinions and data contained in all publications are solely those of the individual author(s) and contributor(s) and not of MDPI and/or the editor(s). MDPI and/or the editor(s) disclaim responsibility for any injury to people or property resulting from any ideas, methods, instructions or products referred to in the content.